

Department of Astronomy - University of Virginia

**Photometric Analysis of Candidate Quadruple
Eclipsing Binary Systems: Dynamical Evolution
of TIC 63459761**

Undergraduate Senior Thesis - ASTR4998

Presented by:
Evan Fagan

Advisor:
Steven R. Majewski

This thesis is submitted in partial completion of the requirements of the BS
Astronomy-Physics Major on 10 May, 2024.

Abstract

Quadruple Eclipsing Binaries [QEBs] are gravitationally bound, hierarchical stellar binaries consisting of at least four bodies, generally corresponding to 2+2 system architecture, though 2+(2+1), 1+(2+1), 2+2+2, etc. arrangements are possible. Single and double eclipsing binary systems are well-known to serve as excellent testbeds for determining stellar and orbital parameters (Torres et al. 2009). QEBs, while exceedingly rare, offer unique opportunities to contribute insights into binary star system evolution and inter-binary interaction. For a significant subsample of the QEB candidate lists derived from the Transiting Exoplanet Survey Satellite (TESS) presented in Kostov et al. (2022) and Kostov et al. (2023), extensive ground-based photometry via the 0.6m Rapid Response Robotic Telescope [RRRT] at Fan Mountain Observatory, VA, and the 0.5m Astrophysical Research Consortium Small Aperture Telescope [ARCSAT] at Apache Point Observatory, NM, in conjunction with speckle interferometry, were obtained to constrain system parameters and identify Eclipse Timing Variations [ETVs]. The program to obtain these observations is described, including a planning tool designed to optimize observing around capturing QEB eclipses. We then describe a systematic error discovered in the determination of distances for QEBs using *Gaia* trigonometric parallaxes, π , for those QEBs resolved by speckle imaging into two subsystems, with the size of that systematic error reaching a peak in ϵ_π/π when the angular separation of the resolved QEB subcomponents becomes comparable to the native resolution of the *Gaia* satellite; clearly *Gaia* astrometry is failing for sources that it marginally resolves. Finally, we focus on a case study of one QEB for which we have extensive multi-epoch observations: TIC 63459761, a 2+2 QEB with primary and secondary orbital periods of 4.362d and 4.244d, respectively, in the Cygnus OB2 association. The degeneracies and potential contributions of various perturbative effects are explored in Section 4, alongside a description of future observations of ETVs and Relative Eclipse Timing Variations [RETVs] that will constrain the system’s architecture.

Contents

1	Introduction	1
2	Data & Background	4
2.1	Ground-based Photometry	4
2.2	Survey Photometry	6
2.3	Speckle Interferometry	9
2.4	Eclipse Timing Variations	10
3	Gaia Distance Discrepancy	12
4	TIC 63459761	14
4.1	Background	14
4.2	Variable Contributions	21
4.3	Planned Observations	22
5	Conclusion	28
6	Acknowledgements	30

Section 1

Introduction

Upwards of 40% of the characterized star systems consist of multiple constituents, meaning the majority of stars exist in hierarchical systems of two or more components (Eggleton & Tokovinin, 2008). This 40% fraction dramatically increases with component mass, with over 70% of massive stars expected to dynamically interact with a companion during their relatively short lifespans (Sana et al., 2012). The comparatively large rate for massive star multiplicity is doubly-favored: increased prestellar gas density, alongside decreased probability of orbital ejection via quasistable configurations or direct interactions on extended ($\tau > 10^8$ year) timescales, promotes both their production and detection. At all mass scales, high-order architectures, with four or more components, are exceptionally rare, constituting only $\sim 2\%$ of known systems, with that fraction drastically diminishing for fifth-, sixth-, and higher-order systems (Eggleton & Tokovinin, 2008).

Quadruple eclipsing binaries [QEBs] form a small subset of this already small, high-order subset. QEBs are hierarchical systems consisting of at least two doubly-eclipsing sub-binaries, each with an orientation of $i \approx 90^\circ$ relative to Earth to produce both primary (α) and secondary (β) eclipses. Hierarchical nomenclature for such systems is $N = \sum_{\Gamma} n_{\Gamma}$, where N is the total number of stellar components, Γ refers to the subsystem index, and n is the number of components of that subsystem. For example, a ‘basic’ QEB, with four components, sorted into binaries each consisting of two stars, is classified as (2+2), though systems with unequal hierarchies, such as in a (3+1) configuration, comprise a significant portion of the $N \geq 4$ population (Tokovinin, 2014, 2021).

Eclipsing binaries [EBs] are well-known to constrain stellar parameters — including orbital period P , relative effective temperature, T_{eff} , relative radii R_{α}/R_{β} , relative stellar radii-orbital semimajor axis $(R_{\alpha} + R_{\beta})/a$, stellar mass ratio q , and the eccentricity-scaled argument of periastron $e \sin \omega$ — through precision time series photometry ((Prša et al., 2011)). The addition of astrometric distances and/or spectroscopic data — e.g., radial velocity time series and/or spectroscopic parallax measurements — can further constrain and characterize these systems. QEBs offer a more complex playground to explore, and contain important information regarding dynamical system evolution, but at the cost of parameter degeneracy. Section 4 explores this characterization difficulty in one particularly complex QEB, TIC 63459761.

The rarity of high-order systems, compounded by the low probability of those systems situated at favorable inclinations, severely limits the sample that can be observed as eclipsing. Regardless, accurate models of QEBs are incredibly relevant to the study of orbit circularization, stellar mergers, type Ia SNe, stellar mass transfer, the Lidov-Kozai mechanism, and other exciting areas of active research in stellar astrophysics (Fang et al., 2018). Large-scale, satellite-based photometric surveys, such as the Transiting Exoplanets Survey Satellite [TESS] (Ricker et al., 2015) and Kepler (Borucki et al., 2010) offer remedy to this issue, their high

Signal-to-Noise Ratio (SNR) capable of identifying minor eclipses and their goliath sample size boosting detection compared to previous, ground-based studies. Data quality is key in QEB studies, as the relative eclipse depth corresponding to the dimmest component will be at-most 50% of its theoretical maximum depth in an isolated EB, thanks to third light contribution from the system's other binary pair. This dilutive effect is exacerbated in systems with uneven hierarchical distributions. While failing to meet the SNR standards of modern surveys, historical ground-based photometric data are sufficient to identify well-pronounced effects such as major eclipses. For example, data from the Wide Angle Search for Planets [WASP] (Butters, O. W. et al., 2010) and the All Sky Automated Survey for SuperNovae [ASAS-SN] (Kochanek et al., 2017) projects are incorporated in Section 4.

Two sets of candidate QEBs produced by a collaboration led by Veselin Kostov, with 97 candidates in a first publication ((Kostov et al., 2022); K22 hereafter) and 101 in the most recent contribution ((Kostov et al., 2023); K23 hereafter) have been derived from TESS data and serve as the basis for this project. While algorithmic methods are capable of identifying an initial sample of QEBs from peaks in Fourier space corresponding to regular, periodic eclipses, human visual inspection is necessary to remove false positives, alongside centroid offsetting in the case of QEBs to confirm contributing sources. The author is a member of a sister EB-and-planet-identification project run through Exogram, a citizen scientist collaboration where candidate EBs are presented with TESS lightcurve data. A preliminary solution, consisting of system period, relative system phase, relative eclipse depths, and eclipse timing variations [ETVs] are included for validation or rejection (Magliano et al., 2023). An example EB candidate evaluated by the author is shown in Figure 1.1.

Photometric survey data, while a boon to (Q)EB study, are insufficient to fully characterize these systems. TESS's massive 21" pixels are unable to resolve arcsec and sub-arcsec separations between constituent QEB pairs. The Earth's atmosphere typical ground-based imaging, imposing an approximate resolution limit of $\sim 1''$ in typical conditions. Diffraction-limited speckle observations by the Majewski et al. collaboration (2024, in preparation), detailed in Section 2.3, can correct for these effects and have resolved subsystem separations as low as 0.0325". While separating constituent stars is beyond current observational capabilities for all identified candidates, 32 have been resolved down to the binary level, constraining inter-binary angular separations, and linear separation when those are combined with a distance estimate.

Section 2.1 overviews the process of ground-based photometry, including observation planning, the data collected from said observations, and the reduction process, while Section 2.2 acknowledges the limitations of survey data that demand ground-based follow-up. Section 2.3 explores the speckle imaging process, as well as its contributions to system characterization. Section 2.4 describes the most common family of ETVs, their source, and how ETV results are presented. Identification of systematic errors in Gaia astrometric parallaxes, peaking at a system separation scale equivalent to Gaia's angular diffraction limit, is investigated in Section 3. The need for near-simultaneous multi-method observation of QEBs is demonstrated with a case study of system TIC 63459761. Rapid evolution over a 17 year timespan, combined with a significant number of confounding effects, has led to past difficulties in modeling the system (Laur, Jaan et al., 2015). An examination of potential contributions to system uncertainty, as well as a suite of future observations to constrain them, is presented in Section 4.

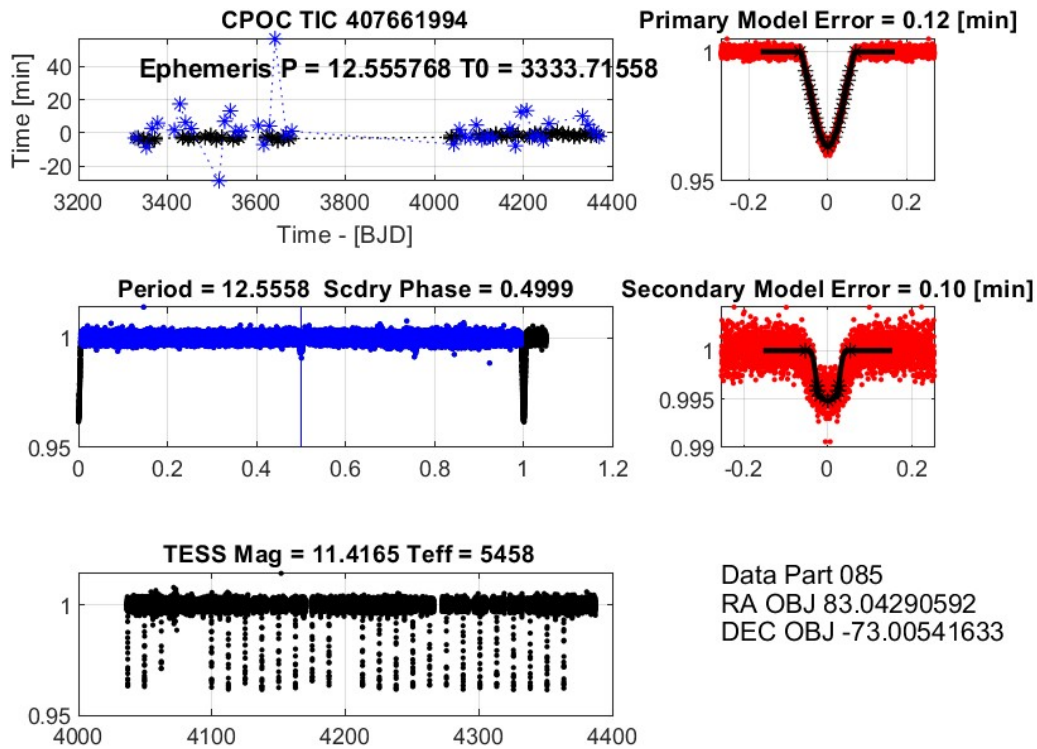


Figure 1.1: Exogram validation page for TIC 407661994, as evaluated by the author. From top left: Observed-minus-Calculated (O-C) diagram (see Section 2.3), tracking ETVs in both α and β eclipses; phase-folded light curve with α shifted to a phase of 1; unfolded TESS light curve showing epoch of observation and preliminary T_{eff} estimate; zoomed plots of both α and β eclipses with best-fit model overlaid and model error. Validation involves confirming that identified eclipses and proposed periods are accurate, as well as identifying false positives, sets of multiple eclipses, and other effects. The advantage of TESS precision and observing cadence is demonstrated through strong identification of a 0.5% eclipse in a $m_{\text{TESS}} = 11.4$ target. Credit exogram.vercel.app.

Section 2

Data & Background

2.1 Ground-based Photometry

Presented in the K22 list of TESS-identified QEBs is the ephemeris — including initial eclipse midpoint, duration, depth, and period — for all eclipses identified with the candidate QEBs. Expected eclipse times could then be calculated by propagating periods forward from the initial midpoint, generating an array of expected midpoints for all 393 eclipse series contained within the catalog for any future dates. However, ground-based observing, limited to nighttime observations and with only a segment of the sky visible on a given night, is not possible for the majority of these predicted eclipses for any particular observing site. To produce a usable planner for each relevant observatory (in our case, the Apache Point Observatory and Fan Mountain Observatory), a python-based sky visibility program was developed to crop impossible observations based on latitude and daily twilight limit constraints. With telescope coordinates, alongside target coordinates, as input, midpoints corresponding to times where the system could not be observed were cut from the preliminary list. To further restrict the sample, ‘possible’ observations were limited only to cases where at least 50% of the expected eclipse duration were visible, or at least three hours in the case of extended eclipses. An additional, optional, minimum altitude condition was introduced to account for the 30° limit of the Rapid Response Robotic Telescope (RRRT) at Fan Mountain Observatory. An example snippet of the produced observation planner is shown in Figure 2.1.

Target	RA	Dec	Tc	P	W	Observable
TIC 375325607 A _α	21 03 10.34	55 28 09.53	1711.9648	1.311984	4.8	2023-08-05 4:58 2023-08-09 3:26 2023-08-10 10:5 2023-08-14 9:23 2023-08-18 7:50 2023-08-22 6:1
TIC 375325607 A _β	21 03 10.34	55 28 09.53	1712.617118	1.311984	3.5	2023-08-07 4:06 2023-08-12 10:0 2023-08-16 8:31 2023-08-20 6:59 2023-08-24 5:27 2023-08-28 3:5
TIC 375325607 B _α	21 03 10.34	55 28 09.53	1719.9224	9.223201	6.9	2023-08-11 11:0 2023-09-08 3:13 2023-09-17 8:35 2023-10-24 6:00 2023-11-02 11:2 2023-11-30 3:2
TIC 375325607 B _β	21 03 10.34	55 28 09.53	1722.902416	9.223201	8.6	2023-08-05 5:19 2023-08-14 10:4 2023-09-11 2:44 2023-09-20 8:06 2023-10-27 5:32 2023-11-05 10:

Figure 2.1: A short sample of the extensive QEB observation table, centered on TIC 375325607, for observing at Apache Point Observatory [APO]. Coordinates are displayed next to the initial eclipse midpoint, T_c , in [BJD - 2457000]; period, P , in days; duration, W , in hours, and a list of dates, in UTC, where a sufficient portion of the predicted eclipse would be visible. Eclipses are identified first by subsystem, A/B/[C], then by primary or secondary, α/β .

Even with a condensed list, the dozens — or more — of possible observations for each eclipse, across hundreds of eclipses, was more than could be observed without a large team of observers and multiple telescopes. To limit observations to targets of high interest, systems marked as potentially exhibiting ETVs in the K22 catalog were prioritized. The sample was further Winnowed to speckle-resolved systems with small separations as well as confidently

TIC ID	N_{APO}	N_{FMO}	S_N	G_{Gaia} [mag]
52856877	210	0	210	10.854
63459761	0	4558	4558	12.1717
161043618	1798	0	1798	12.2735
200094011	429	6	435	9.7108
201310151	180	0	180	14.8844
219469945	0	439	439	12.421
239872462	0	1435	1435	11.2879
260056937	875	0	875	10.1611
266771301	520	0	520	12.2552
292318612	0	1504	1504	14.1346
307119043	3137	2550	5687	10.0128
367448265	2568	11852	14420	7.9098
414969157	0	906	906	14.062
443862276	244	0	244	14.0569
470710327	1452	5569	7021	9.7874

Table 2.1: From left: candidate TESS identifier; number of observations via ARCSAT; number of observations via RRRT; total number of observations; apparent magnitude in Gaia G passband. Observations span between October 2023 and April 2024. Unreduced data available upon request.

unresolved systems (see Section 2.3), producing a final list of 15 prime QEB targets (see Table 2.1).

Candidates from this concentrated sample were observed with the 24inch RRRT at Fan Mountain Observatory [FMO] in Coveseville, VA, and/or the 0.5m ARCSAT telescope at APO in Sunspot, NM (Salgado & McDavid, 2008). While a small number of frames were taken in alternate filters to test relative eclipse depths across colors, the majority of observations were taken in the best-available center optical passband, the Johnson-Cousins V filter on the RRRT and the SDSS g filter on ARCSAT. The number of observations collected from each observatory, as well as the out-of-eclipse Gaia G magnitude, are listed in Table 2.1.

The majority of the photometric reduction was completed using the AstroImageJ software (Collins et al., 2017), with some observations reduced via the in-browser Afterglow program (Meredith et al., 2020). Both software packages allow for multi-aperture photometry, where time series measurements of relative photometry against multiple comparison stars is possible, with the latter input as a target list. The observed variance in comparison stars is then used to correct for atmospheric effects, producing a normalized light curve for the target. While this approach can even correct for homogenous weather effects, like haze or dust, thin clouds that fail to uniformly obscure the entire frame produce significant noise. An example AstroImageJ light curve, with observations from the RRRT, is shown in Figure 2.2.

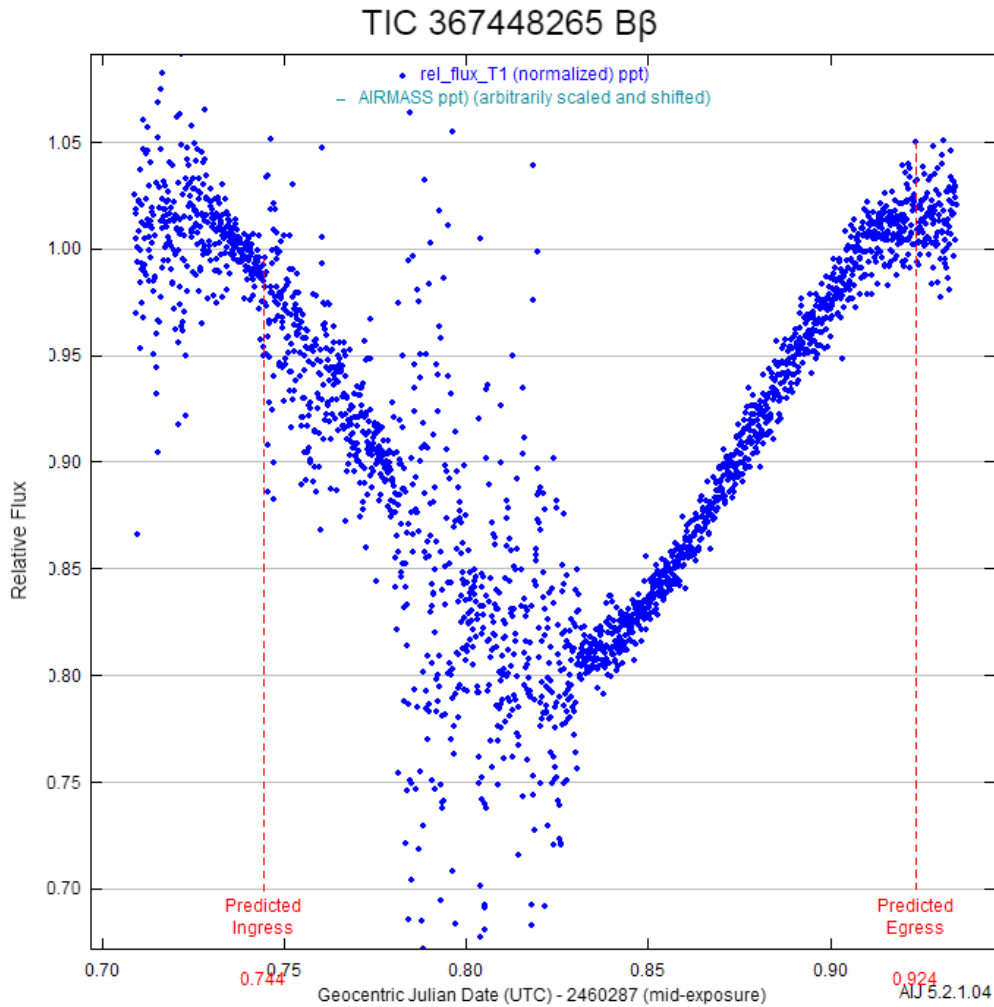


Figure 2.2: A $B\beta$ eclipse of TIC 367448265, observed via the RRRT on December 8, 2023. The predicted ingress and egress, based on the TESS-derived ephemerides in K22, are calculated by subtracting/adding half the eclipse duration to the expected midpoint and are marked. The significant scatter and low SNR of the first half of the observation is due to thin clouds, while the second half corresponds to a period of much better skies and therefore produces a much better determined light curve.

2.2 Survey Photometry

Follow-up photometry is labor-intensive, in preparation, observation, and reduction, but necessary to validate QEB candidates. Low angular resolution survey data, especially in crowded fields, struggles to separate nearby sources, thereby introducing significant uncertainty and, in some cases, producing ‘ghost’ light curves that can result in false positive QEB detections. While methods like centroid fitting, wherein the relative measured positions of the source in, and out, of eclipse are compared to test for false detections, attempt to correct for local source contribution, low resolution ground and satellite surveys still suffer from spillover for clustered sources (Hedges, 2021). As a result, multiple close sources can exhibit the same variable behavior, matching eclipses and other brightness modulations. Figure 2.3 and Figure 2.4 demonstrate this issue in the case of sources around TIC 63459761, which sits in the packed Cygnus OB2 association, with both TESS and WASP data, though the same validation was applied to other

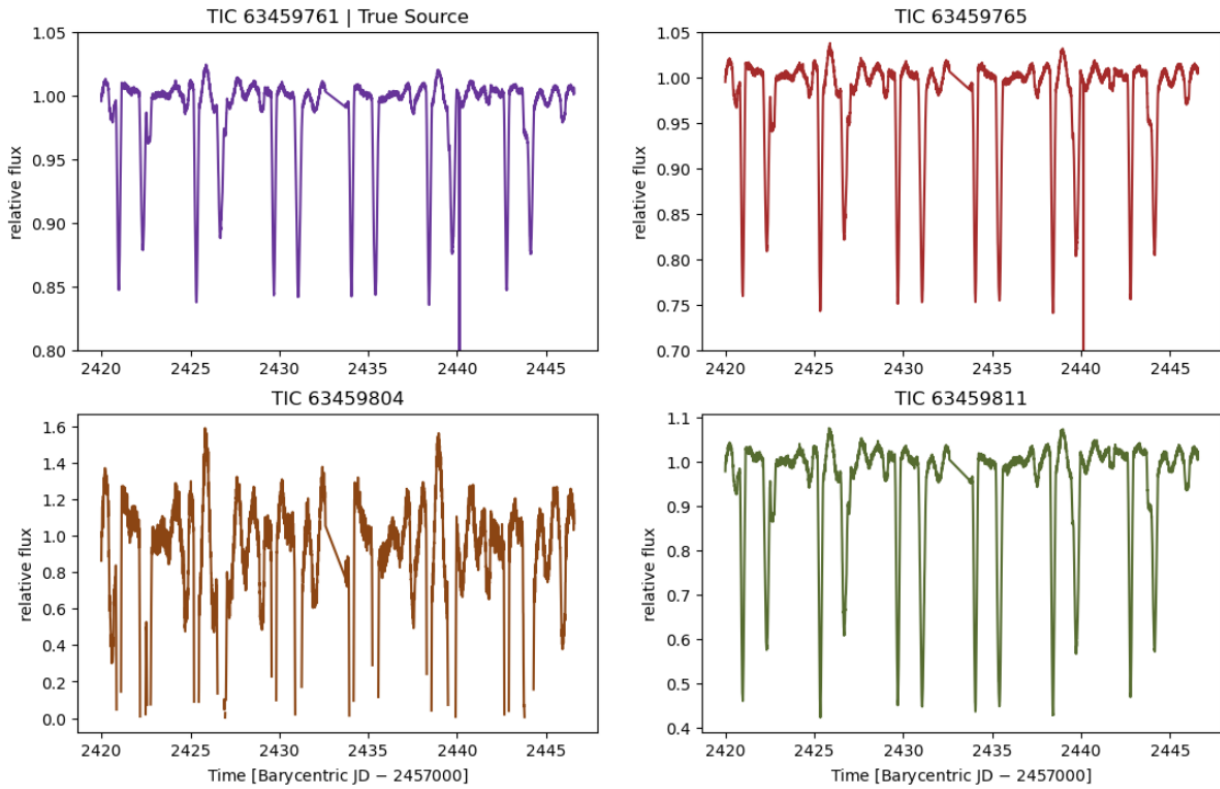


Figure 2.3: Quick-Look Pipeline (QLP) light curves for TIC 63459761 and three sources in its immediate vicinity, observed in TESS Sector 41, 2021, with 600s exposure time. Note that while the depths of both eclipses and out-of-eclipse variations correspond to different changes in relative flux between observed sources, the structure of the variations and the relative depths between eclipses are internally consistent.

targets in the QEB sample.

These photometric errors are not a problem for a telescope with even a moderate resolution limit. A frame from this field observed via the RRRT in the V passband is shown in Figure 2.5. Follow-up photometry not only addresses the issue of precise identification of the actual eclipsing source, but also offers more precise bounds on the true eclipse depths and variations by eliminating the third light spillover effect from a source’s neighbors, which then, in turn, provides a more accurate baseline flux and magnitude. Together, these survey-specific issues justify the supplementary use of precision ground-based photometry. This is not to discount the essential contribution of data from sources like TESS; on the contrary, working together the TESS photometry supplemented by ground-based photometry provides a powerful avenue for not only more accurately characterizing the true depths of lightcurves, but also their color variations, and their changes over time (i.e., ETVs).

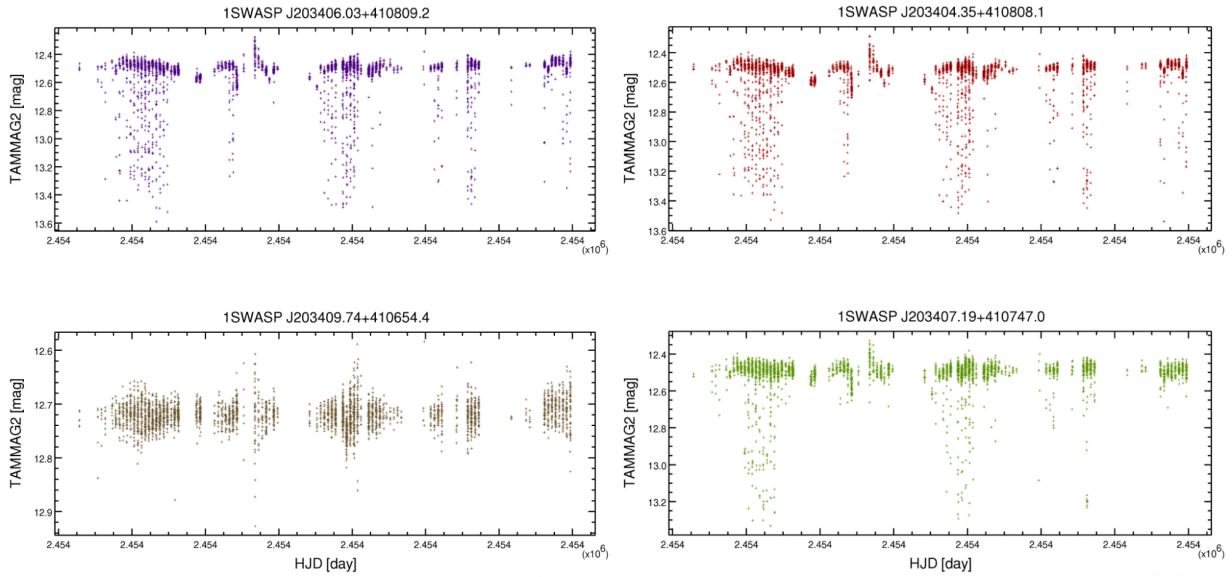


Figure 2.4: SUPERWASP light curves for the same set of sources as Fig 2, with WASP TAMMAG2 [mag] plotted against Heliocentric Julian Date, with those shown corresponding to 2007. TIC 63459804, located bottom-left, displays a light curve consistent with an unaffected, constant point source observed by WASP. Plotted using the NASA Exoplanet Archive data visualization tool (Butters, O. W. et al., 2010)

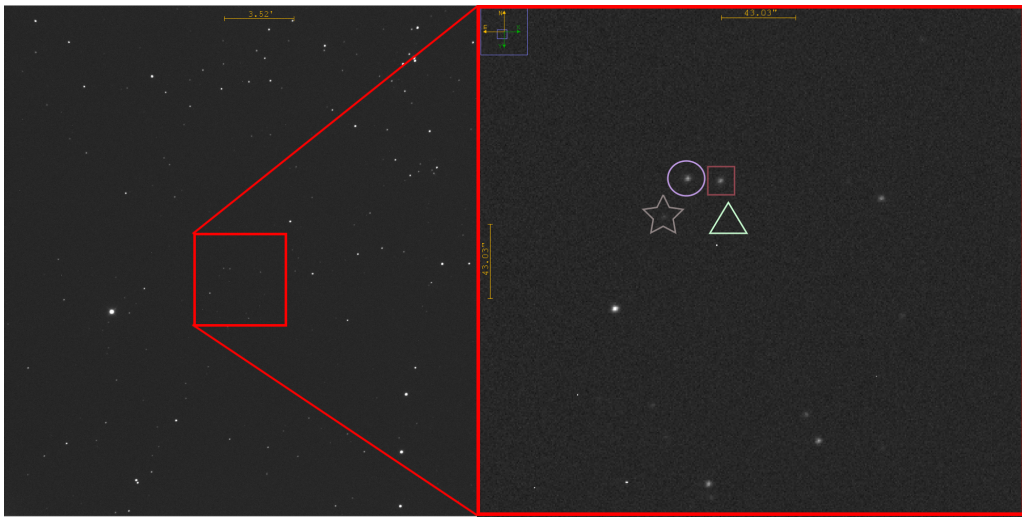


Figure 2.5: Source field observed with the RRRT in the Johnson-Cousins V passband, with a 6 second exposure time, with the right panel showing a magnified view of the boxed region on the left. The circle, square, star, and triangle contain the sources TIC 63459761, 63459765, 63459804, and 63459811, respectively. Target sources appear dim due to the short exposure, chosen to avoid saturation of the bright source HD 196241 ($m_V = 6.65$), seen to the left of the zoomed region (Høg et al., 2000).

2.3 Speckle Interferometry

Precision photometry offers important information, but plain imaging, where possible, is an ideal supplement for determining system parameters. However, atmospheric effects leads to variation of point sources, their focused position, shape, and appearance on a detector changing on frequencies of order $1e3+$ Hz at optical wavelengths, with exact timescale depending on wavelength (Dainty, 1981). An incoming wavefront is inevitably distorted as it travels through the atmosphere, with a more turbulent atmosphere resulting in greater inconsistencies between successive wavefronts. Image wander, imposed by the tilting of a wavefront relative to an aperture, scintillation, brightness variations induced by the variable refractive index of the atmosphere, and image blurring, resulting from contributions of multiple wavefronts, all alter or degrade traditional ground-based observations. An extended exposure of a source produces a point-spread function [PSF], a Gaussian distribution of speckles: individual Airy disks produced by isoplanatic patches, which are small (~ 10 cm) atmospheric cells wherein wavefront distortion is consistent. This introduces a site-dependent long exposure resolution limit of $\sim 1''$, even for telescopes with theoretical resolution limits far below that range.

However, two close sources, their passing through the same isoplanatic patches, will experience the same distortion. For example, if two sources are separated by $0.5''$, each speckle will consist of two Airy disks separated by $0.5''$, even if the position of the speckle on the imaging plane changes. While extended exposures will capture an extended, smooth PSF, legible groups of speckles can be captured with short exposures (Greenaway, 1981). By converting multiple fast images into Fourier space, consistently present distances between points — for example, in the above hypothetical, separations of $0.5''$ — will be overrepresented compared to random noise. A single diffraction-limited image can then be reconstructed, containing the original information on both source separation and relative orientation.

A complete speckle survey of the K22 + K23 catalog is currently underway as part of the Majewski et al. collaboration, of which the author is a member, using predominantly the Differential Speckle Survey Instrument [DSSI] (Horch et al., 2009) and hopefully other instruments. In the so-called “speckle-resolved systems”, while the binaries themselves, A and B, may be separated, their constituents, A_α , A_β , B_α , and B_β , remain unresolved in all cases. The angular separation between A and B can be combined with the distance to the system to determine the projected linear separation between A and B. Changes in separation and orientation angle over time, determined by multiple speckle runs, can begin to map out the projected orbit of A and B about their shared barycenter, in the case they are gravitationally bound, though a complete orbit would require decades of observations — or centuries — in most cases. Partial breakdown of the QEB into subsystems also gives component binary magnitudes, while speckle observation during eclipse can constrain true eclipse depths, rather than the relative depths from photometry of their combined flux.

Even at the theoretical maximum resolution on 3.5-4m telescopes, corresponding to approximately $\sim 0.03''$ for mid-optical wavelengths, both distant and/or tightly-bound QEBs are inseparable. Speckle resolvability is dependent on relative magnitude, with high $\Delta m_{A;B}$ components being more difficult to resolve than two similarly bright components. However, maximum $\Delta m_{A;B}$ is bound to low order by the observation of both sets of eclipses, with the minimum possible flux contribution from a dimmer binary equal to the depth of its deepest eclipse. For example, a 5% eclipse in the higher magnitude system, assuming no flux contributions aside from the QEB, imposes a maximum $\Delta m_{A;B}$ of ~ 3.2 , while even a 1% eclipse imposes a maximum $\Delta m_{A;B}$ of ~ 5 . Confidently unseparated QEBs are classified as High Quality Non-Detections (HQNDs), with maximum angular separation and distance imposing an upper bound to linear projected system separation.

That separation is also bounded from below by the semi-analytical stability criterion. A

binary system with a tertiary companion — in the case of QEBs, the other binary — is stable for tertiary orbits that are significantly larger than the binary separation, satisfying the following conditions via Mardling & Aarseth (2001):

$$a_p/a_c \geq 2.8(1 + m_p/m_c)^{2/3}(1 + e_p)^{2/5}(1 - e_p)^{-6/5}(1 - .3\iota/\pi) \quad (2.1)$$

where a_p , m_p , e_p are the semi-major axis, mass, and orbital eccentricity of the perturber; a_c , m_c are the semi-major axis and combined mass of the binary, and ι is the relative inclination of the perturbing orbit to the binary orbit, in radians. This rough condition would have to be satisfied from the reference frame of both A and B subsystems, with a_p and e_p consistent. Since the destabilizing effects of a second, extended binary system are greater than those from a perturbative point mass, the system separation would in turn have to be larger than this prescription provides. The effects of gravitationally bound systems upon each other can be expressed as ETVs.

2.4 Eclipse Timing Variations

The identification and modeling of ETVs are of special interest in QEBs. In an unperturbed, minimally-interacting EB, both eclipses, α and β , will repeat on a regular, shared cadence corresponding to the orbital period. However, if an unseen tertiary object also orbits the binary, usually on a significantly longer period, the overall system barycenter will modulate with the progression of that tertiary orbit. This produces a periodic Light Travel Time Effect (LTTE) in the central EB, causing eclipses to occur earlier or later than expected depending on the phase of the tertiary (Zasche, P. et al., 2016). This appears as periodic effects in an (O-C), or observed-minus-calculated, curve, which plots the difference between observed eclipse time and predicted eclipse time, calculated from initial ephemeris, as a function of time or orbital periods. The magnitude and shape of an LTTE-induced (O-C) curve can restrict tertiary orbital parameters, such as tertiary velocity, inclination, and eccentricity. LTTEs, conveniently, are (O-C)-consistent for both α and β eclipses for a given system in both phase and magnitude. Therefore, if ETVs in both α and β can be fit to the same (O-C) curve, they're attributable to LTTE. Periodic variations in the primary eclipse of the A subsystem of TIC 370440624 are shown in Figure 2.6, along with a sinusoidal fit. It should be noted that real LTTE (O-C) curves are skewed periodic functions, not even functions; however, their determination requires sampling from multiple regions in a given perturbing period, which limits the use of irregular data from sources like TESS in some cases. Dynamical, non-LTTE effects are further examined in Section 4.

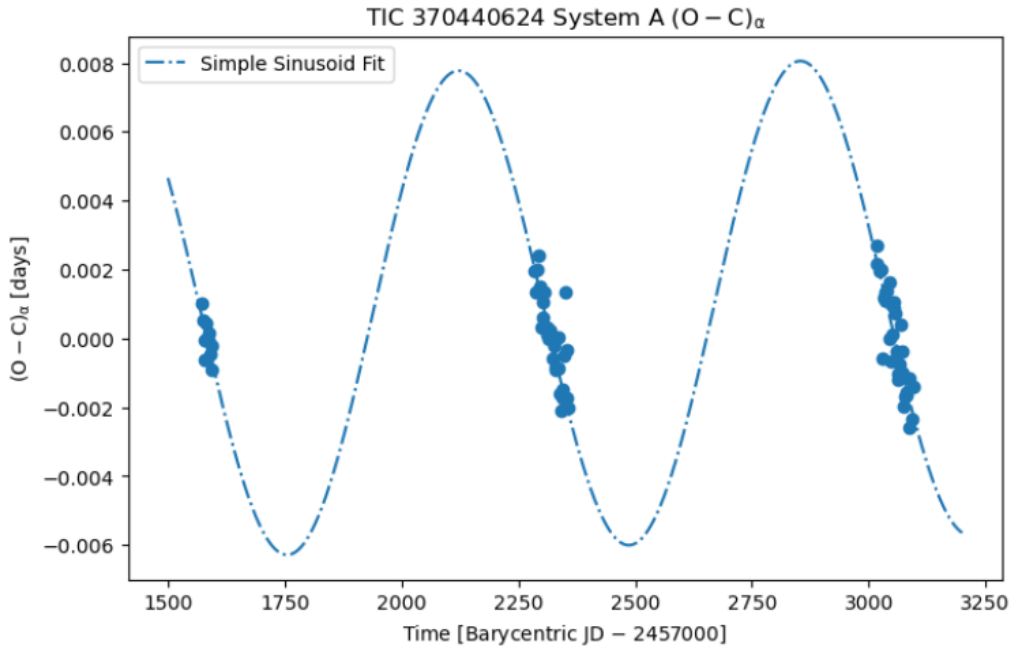


Figure 2.6: (O-C) curve for TIC 370440624 $A\alpha$, orbital period $P = 2.2351\text{d}$, with data spanning across three TESS sectors, showing periodic variations in eclipse timing. Perturbing periods that happen to roughly align with TESS sector cadence introduce Nyquist degeneracy in ETV modeling, as only one section of a predicted (O-C) curve is observed. Any periodicity derived from repeated observations of the same (O-C) segment is thus tentative. Speckle observations characterize this particular system as an HQND, with maximum A-B separation of 33 AU, though the ~ 700 day periodicity exhibited suggests a much smaller separation. A rough sinusoidal fit is overlaid, though is not necessarily representative of the complete curve.

Since ground-based observations are limited only by telescope time, sky position, and weather, the combination of semiregular eclipse timing measurements, combined with the high-density results from active TESS sectors, can well-define a given system’s (O-C) curve. With the smallest speckle-resolved QEB system separation being approximately 24 AU (TIC 292318612), most variational timescales are longer than well-constrainable within the 7-month timescale of observation undertaken for this project. However, while the smallest HQND-derived maximum separation is 18 AU, the true separations of HQNDs may be lower, corresponding to (O-C) variations that may fall within an observable epoch. The aforementioned 18 AU maximum separation corresponds to TIC 454140642, which was characterized by Kostov et al. (2021a) with a separation of 1.86 AU, corresponding to a 432.1 day orbit. HQNDs thus form a shortlist for systems with potential year-scale ETVs, and planned future observations—both photometric and spectral—will focus on these candidates, filling out their space of ETV contributions.

Section 3

Gaia Distance Discrepancy

The high-precision astrometry provided by the *Gaia* mission is the gold standard for obtaining distances to nearby stars via trigonometric parallax (Gaia Collaboration et al., 2023). Estimating the distances to QEBs through other means, such as through photometric or spectroscopic parallaxes, is challenging given that the complex convolution of the spectral energy distributions by the 4+ constituent stars of a QEB; therefore a more direct measurement through trigonometric parallax should be optimal. However, while using resolved speckle angular separations to determine projected linear system separations, a correlation between *Gaia* relative parallax error and system separation was observed. Figure 3.1 shows *Gaia* parallax error, normalized to parallax, versus speckle-imaging-derived angular separations.

Visual binary separation in *Gaia* DR3, while improved from previous releases, is a known issue discussed in Section 2 of Fabricius, C. et al. (2021). While DR2 is advertised as reaching an effective angular resolution of $0.4''$ (Gaia Collaboration et al., 2018), and DR3 is described as having improved this result, an updated value for effective *Gaia* resolution is not offered. *Gaia*'s ability to resolve system components beyond $0.7''$ is well-reflected when plotting parallax error against the speckle-derived separations, with its astrometry seemingly confused by almost resolved, marginally point-like sources at the limits of its effective resolution. The effects of this same-source crowding on *Gaia* astrometry results are underexplored, and a comparison with a known visual binary catalog on parallax error should be completed to identify any systematics on derived parallaxes, thus distances. As a caveat, QEB system separations at the time of the *Gaia* observations is not precisely determined; in general, speckle results over multiple epochs reveal separation variations on order $0.01''$ in some systems, so that the exact separation during *Gaia* observation is inconclusive. However, we anticipate that this effect should be insignificant over the relatively short epoch of *Gaia* observation.

The distance ambiguities induced in QEB systems near the minimum *Gaia* resolution thereby limit the applicability of trigonometric parallax to their characterization. Of the 18 observed QEB systems with $\epsilon_\pi/\pi > 10\%$, one corresponds to an unresolved HQND, and the rest correspond to resolved systems with sub- $0.7''$ separation. With growing QEB candidate lists (K23; Zasche, P. et al. (2019)) and limited observing time, such high-error systems may be pointers to a set of likely-resolvable observations. In the other direction, mapping out the low-separation ($< .05''$) range could identify at what scale *Gaia* systematics reduce to random noise. The visual binary separability curve in Fabricius, C. et al. (2021), Figure 7, shows a small increase in resolved systems below $0.4''$ and these authors noted a lack of explanation for this effect. By utilizing characterized HQND QEBs to calculate projected angular separations on the sky, Figure 3.1 can be extended past the speckle-observable limit, which can then be used to help identify the unexplained *Gaia* behavior, improving future data releases.

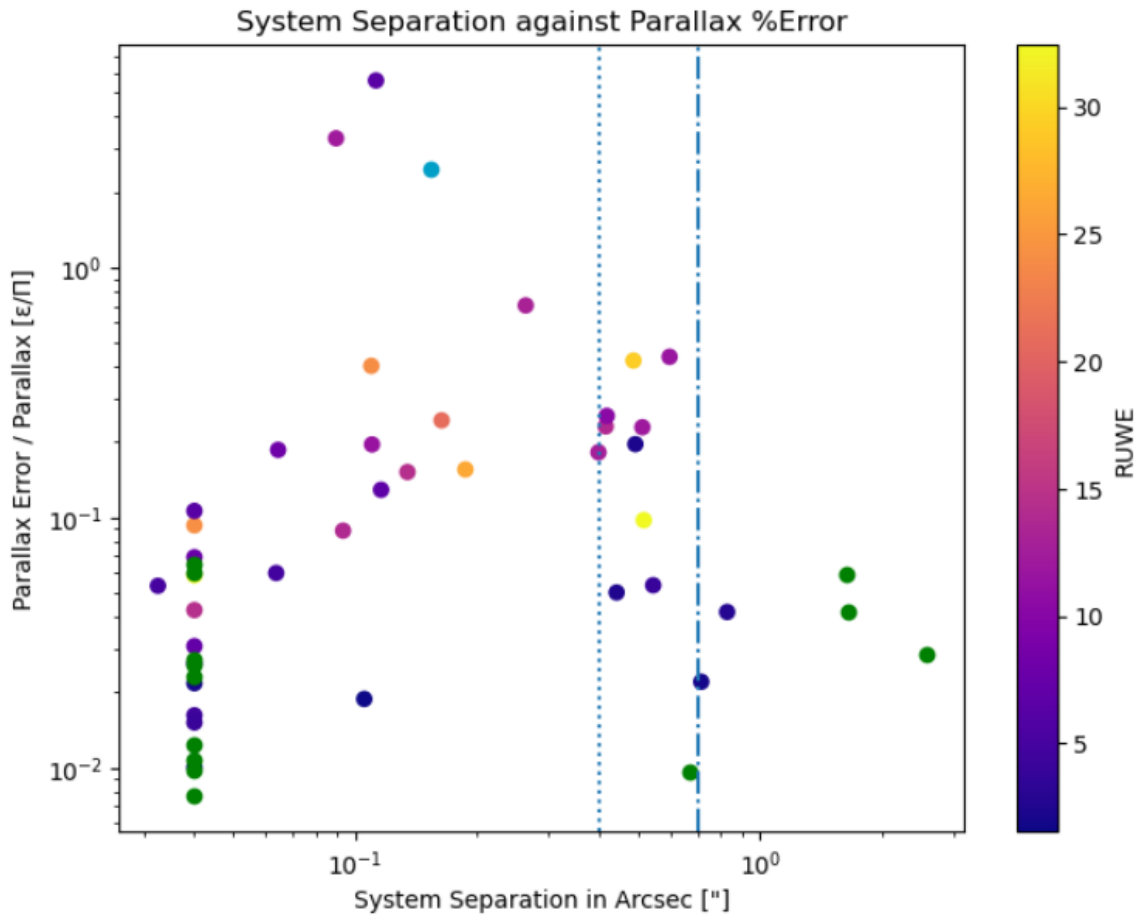


Figure 3.1: QEB system angular separation versus relative parallax error, ϵ_π/π , on a log-log scale. The line of points at separation = 0.04'' consists of HQNDs, assigned a separation corresponding to the approximate resolution limit for our speckle interferometry on a 3.5m telescope. Green points correspond to objects with *Gaia* RUWE ≤ 1.4 , which are sources for which *Gaia* is able to well-fit a single-star solution to describe observations (Fabricius, C. et al., 2021). The cyan point corresponds to TIC 389836747, which lacks an associated RUWE within *Gaia* DR3. The dotted/dashed lines at separations of 0.4''/0.7'' correspond to the approximate angular resolution achieved by *Gaia* DR2 and therefore the visual binary completeness limit of *Gaia* DR3 (Gaia Collaboration et al., 2018) (Fabricius, C. et al., 2021).

Section 4

TIC 63459761

4.1 Background

Because QEB system evolutionary timescales are proportional to the inter-binary orbital period, which is in turn proportional to the system separation through standard Keplerian mechanics, speckle-derived HQNDs are more likely to display observable dynamical changes over short time periods. While the upper system separation bound of TIC 63459761 is on order 100 AU, thanks to its location in the 1570_{-70}^{+80} pc Cygnus OB2 association (Rate et al., 2020), this QEB's high-magnitude ETVs, first suggested in the K22 catalog, combined with a historical record of observations spanning multiple decades, make it an enticing target to explore in greater depth.

Initially identified as object 720 in the Massey & Thompson (1991) catalog (referred to as MT91 720 or MT720 in literature), TIC 63459761 was characterized as a B star with no unusual characteristics. The extended RV survey undertaken in Kiminki et al. (2007) between 1999-2005 updated the classification of this source to O9.5V, and noted the presence of three separate, approximately equivalent, sets of spectral lines, and proposed a triple system solution. Updated measurements from a subsequent survey present a complete RV curve for the system, constraining the central binary to B0-1V and B1-2V components (Kiminki et al., 2012).

Its abnormally high eccentricity, a precise orbital period, as well as mass and inclination bounds, are noted in this study. A minor discrepancy in the provided heliocentric RV curve, shown in Kiminki et al. (2012), Figure 13, features secondary star RV values near orbital turning points ($K_{\beta,max}$; $K_{\beta,min}$) above the model line, including when considering errors. Their figure is reprinted here as Figure 4.1.

Analysis of this source continued with photometric variability studies, which first identified its eclipsing, and double-eclipsing, status in Salas et al. (2014), where the system is designated as ALS 15 146. The photometric study in Kobulnicky et al. (2014) derives a period of 4.0677d with high confidence, but this result is inconsistent with both current as well as concurrent observations, and is thus not considered in this analysis. The system was modeled, using new photometric data and RV measurements from Kiminki et al. (2008), by Laur, Jaan et al. (2015) as part of a binary mass loss study. Component determination via the PHOEBE binary modeling software offered the first parametric characterization of the system, listed in Table 4.1.

This model was able to correctly identify a few quirks of the system, key among them a reversal of eclipse depths. Rather than the deepest eclipse corresponding to the occultation of the primary star α , it corresponds to the passage of α in front of β , with the shallow eclipse, β occulting α , underexpressed due to the relatively high inclination. As a visual aid, Figure 4.2 displays the approximate system structure under these parameters.

However, this binary model fails to reproduce a number of observed system parameters, in

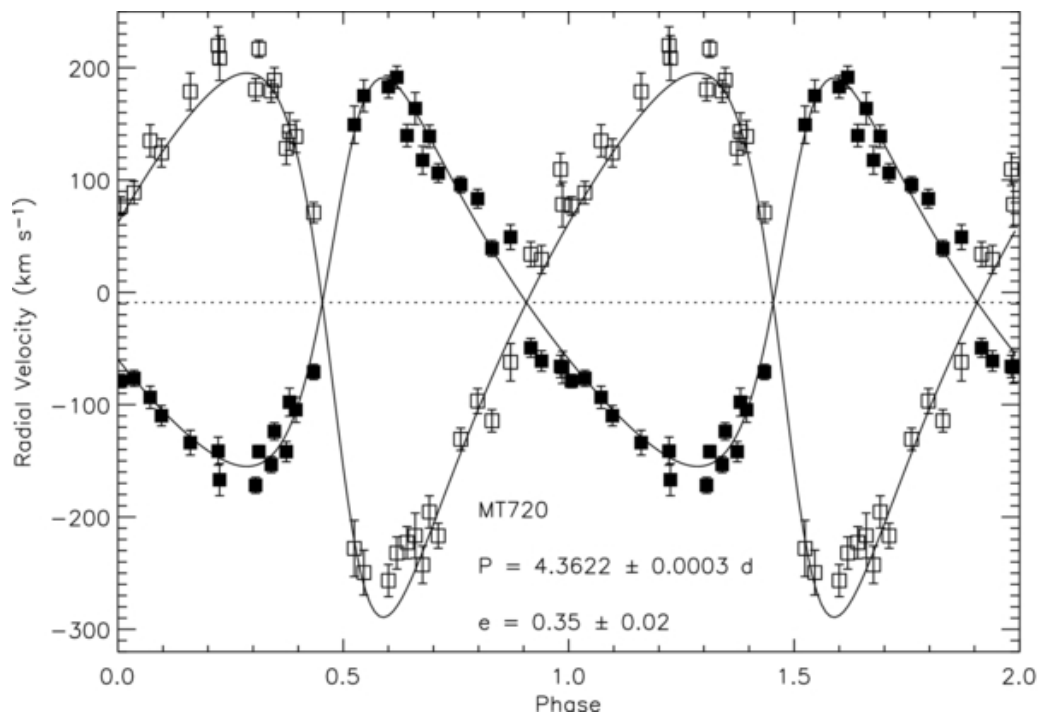


Figure 4.1: Figure 13 from Kiminki et al. (2012), with original caption “Heliocentric radial velocity curve and orbital solution for MT720 using 32 of the highest S/N spectra obtained at WIRO with WIRO-Longslit.” Additional comments: While the primary RV measurements (filled squares) strongly fit the predictions of a 2-component system, with symmetric residuals, the secondary RV measurements (open squares) skew positive at both turning points, suggesting deviation from the simple binary model.

Parameter	PHOEBE Value	Error
$M_\alpha [M_s]$	18.52	1.51
$M_\beta [M_s]$	13.19	1.07
q	0.71	0.03
$R_\alpha [R_s]$	9.93	0.59
$R_\beta [R_s]$	8.47	0.38
$T_\alpha [K]$	29800	<i>FIXED</i>
$T_\beta [K]$	19202	80
i [o]	71.09	0.28
a [R_s]	35.52	0.78
e	0.34	0.005
$\omega [^\circ]$	298	<i>N/A</i>
Spectral Class	B0-1V + B1-2V	<i>N/A</i>

Table 4.1: PHOEBE best-fit parameters for the TIC 63459761 A subsystem, from Laur, Jaan et al. (2015) Stellar characteristics — mass, radii, temperature — are determined for both α and β , while orbital parameters — i, a, e, ω — are derived for the A system. Note that these parameters correspond to an eclipse period of 4.32d, while the observed periodicity — including in the study — has remained consistent at approximately 4.362d.

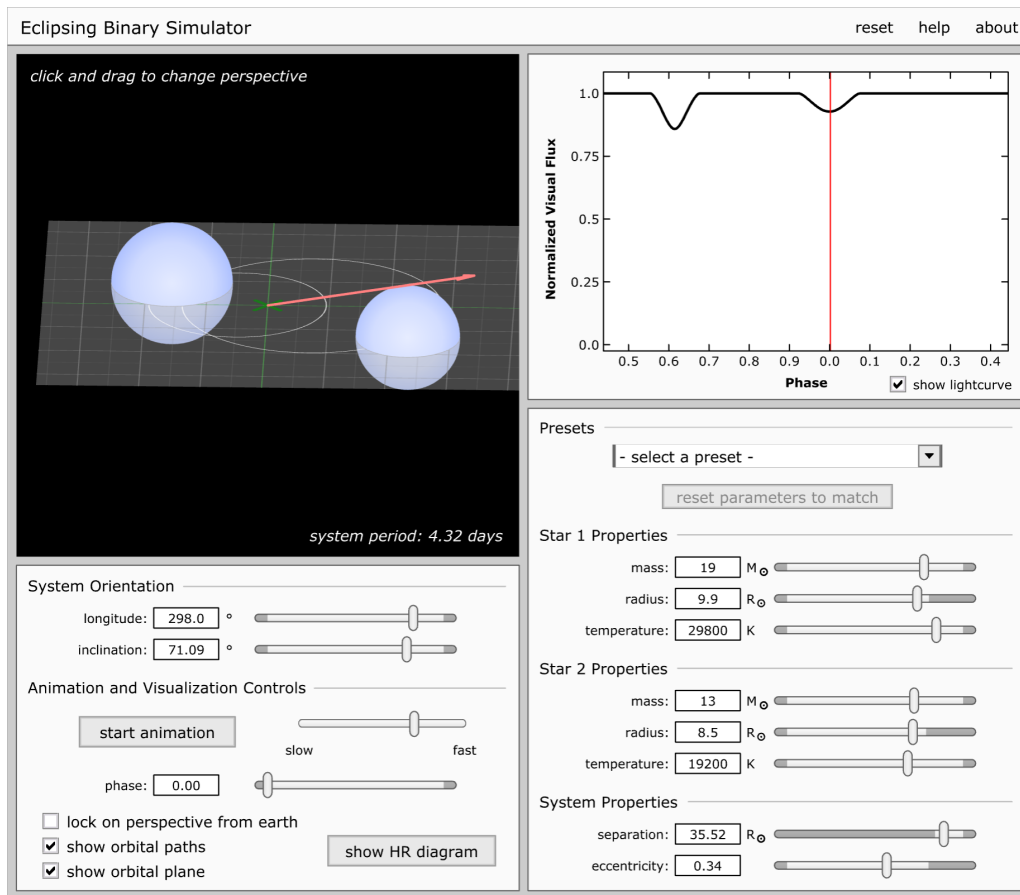


Figure 4.2: Simple simulation of TIC 63459761, via NAAP Labs’ Eclipsing Binary Simulator applet, accessible at (<https://astro.unl.edu/naap//ebs/animations/ebs.html>). Input parameters taken from Laur, Jaan et al. (2015). The red arrow corresponds to the direction of Earth.

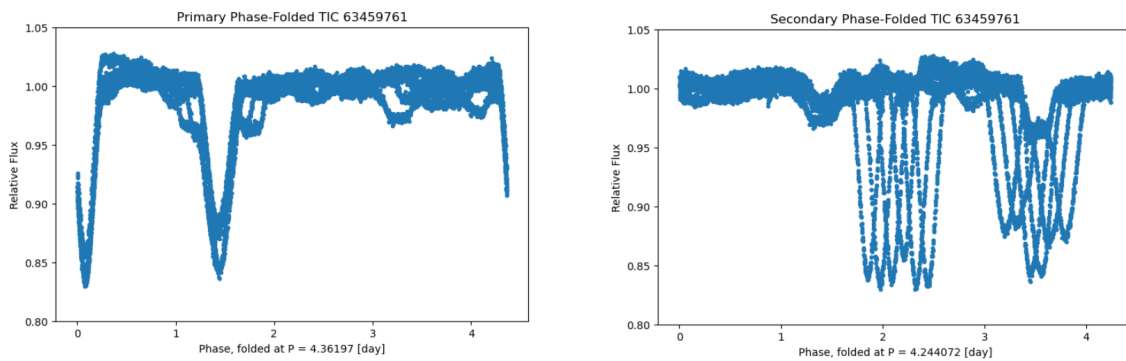


Figure 4.3: Phase-folds of TESS sectors [14, 55, 74] observed during the years [2021, 2022, 2024], respectively. The large interference in the second plot stems from the near-resonance of the two orbital periods, with the real secondary system eclipses located at phases of approximately 1.3d; 3.5d. The inconsistent baseline when folded stems from periodic flux modulations.

some cases reversing direction for rates of change. High mass transfer (of order $10^{-4} M_{\odot}/\text{year}$) is both predicted by the model and fits the empirical data, but said data predicts mass gain in α while the model predicts mass loss (Laur, Jaan et al., 2015). Period evolution is also reversed in the same manner, with no overlap between positive observed period change and negative predicted period change, as is displayed in Laur, Jaan et al. (2015), Figure 4. The observed eclipse width for eclipse β is also inconsistent with predictions, with the observed eclipse being thinner, corresponding to an underpredicted $e\sin\omega$. These errors are ascribed to photometric noise in Laur, Jaan et al. (2015), but align with dynamical evolution between the epoch of RV and photometric observations.

TIC 63459761’s inclusion in the TESS Target of Interest [TOI] list has allowed for an expanded scale of photometric observations in recent years, and led to the source’s inclusion in the K22 catalog. Improved resolution and error correction led to the identification of a second set of eclipses, corresponding to a 4.2441d orbital period with low eccentricity. The near synchronicity of this orbital period with the primary system orbital period may have led to the miscalculated period in Kobulnicky et al. (2014), with eclipses identified in frequency-space over limited data producing false power peaks. Ellipsoidal variations were also identified in the system, though a simple phase-fold on either period reveals disagreement between the periodicity of ellipsoidal variability and the period of either system. Example attempted phase-folds, added over multiple TESS sectors, are shown in Figure 4.3.

Noting the mismatch between quiescent variations in eclipse-folded phase-space, the present author speculated that there may be third light contributions from an ellipsoidal variable within the field. The contribution of various periodicities can be mapped via a Lomb-Scargle periodogram, shown in Figure 4.4.

As expected from noisy data with two sets of eclipsing binaries, the power spectrum features strong expression at integer harmonics of the orbital frequency at low values. However, the small expression at roughly three times the primary period appears out of place, something we initially ascribed as a bias effect from TESS’s roughly month-long observations. To not leave discrepancies unobserved, vertically-separated phase folds for the three later sectors of TESS SPOC data, folded on $P_A = 4.36197\text{d}$, $2P_A$, and $3P_A$ are shown in Figure 4.5.

Within the out-of-eclipse flux, a dominant sinusoidal component with an amplitude of $\sim 2\%$ is well-expressed, repeating 14 times within the 3rd harmonic period $3P_A$. This periodicity is marked in Figure 4.4. Its amplitude, however, as well as its position relative to eclipses A_{α} and A_{β} , modulate within that range, rather than the consistent double expression per orbit one would expect from a standard ellipsoidal variable.

The first subplot in Figure 4.5 also displays the other core abnormality of TIC 63459761:

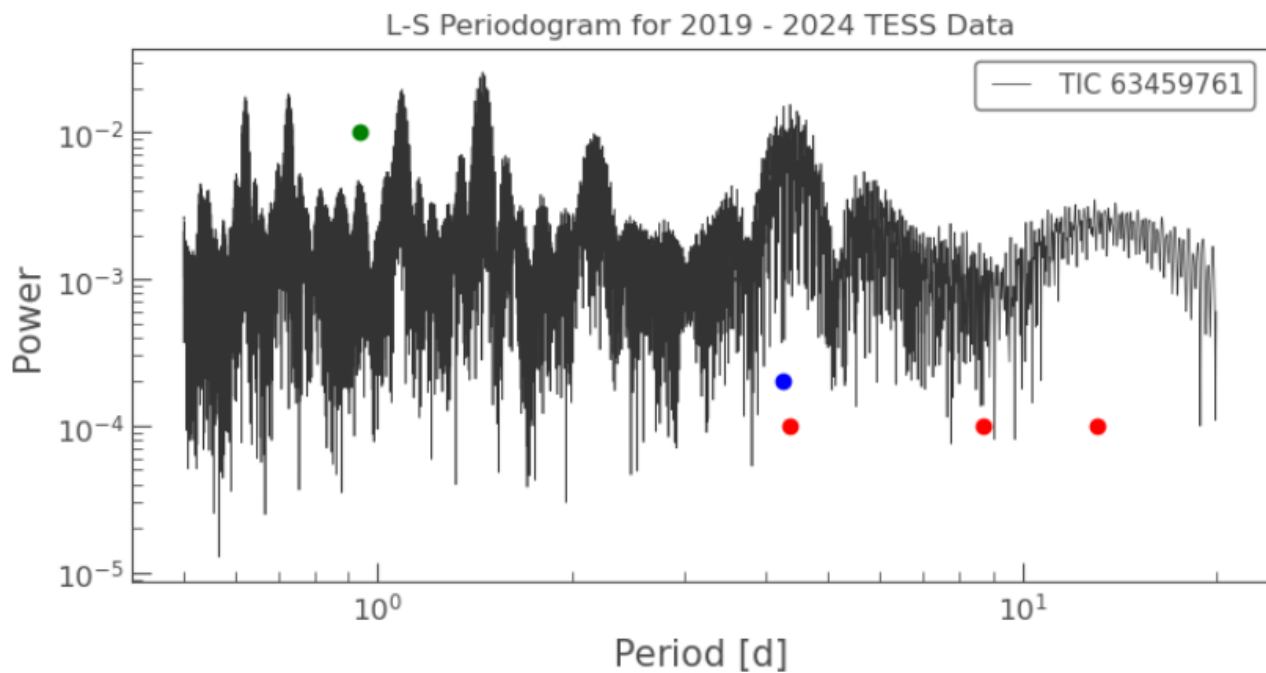


Figure 4.4: Lomb-Scargle periodogram for four sectors of TESS Science Processing Operations Center pipeline [SPOC] data, corresponding to the years [2019, 2021, 2022, 2024]. The widened peak at ~ 4.2 days corresponds to the contributions from both pairs of eclipses, while the lower peaks at power order 10^{-2} correspond to frequency harmonics of the orbital periods. In red are the first, second, and third period harmonics of the A subsystem period, while in blue is the orbital period of the B subsystem. The green point corresponds to minor expression at $(3/14)P_A$, matching the short-term periodicity of ellipsoidal modulations.

Eclipse \ Year	2019	2021	2022	2024
α	0.121871	*0.136006	0.134543	0.134298
β	0.168887	0.159625	0.161522	*0.171644

Table 4.2: Relative eclipse depth (baseline normalized to 1) for α ; β eclipses across TESS sectors. Values marked * correspond to sectors where multiple eclipses were subject to significant B-induced interference, producing artificially deepened depths, though every sector had some degree of interference.

relative phase evolution. While a consistent period well-folds all three light curves with respect to eclipses internally, the separation of eclipse A_α (shallow) and A_β (deep) is decreased in later times, represented by a leftwards wander in phase-space. Phase Variations [PVs] are a subclass of ETVs that correspond to effects other than standard LTTE.

The relative time between eclipses in an EB is described by a family of “difference functions,” their exact forms varying in the literature, with the low-order-in-eccentricity expansion most common. Due to the significant eccentricity required to explain the relative phase observed in TIC 63459761, however, the fifth order expansion via Sterne (1939) is used for precision:

$$f(\omega, e) = (t_\beta - t_\alpha)/P \quad (4.1)$$

$$f(\omega, e) = (1/2\pi)(4e\cos\omega - (2e^3/3 + e^5/4)\cos3\omega + (3e^5/20)\cos5\omega + \dots) + 1/2 \quad (4.2)$$

where t_β ; t_α correspond to the timings of secondary and primary eclipses, and dividing by the orbital period gives a unitless phase of eclipse β relative to α at 0. A given relative phase corresponds to a surface in parameter space that uniquely defines pairs of apsidal position (ω) and eccentricity (e), shown in Figure 4.6. The derivative of $f(\omega, e)$, corresponding to the phase evolution of the system as a function of time, is shown below.

$$K_e = (4\cos\omega - (5e^4/4 + 2e^2)\cos3\omega + (3/4)e^4\cos5\omega) \quad (4.3)$$

$$K_\omega = (-4e\sin\omega + 3(e^5/4 + 2e^3/3)\sin3\omega - (3e^5/4)\sin5\omega) \quad (4.4)$$

$$df(\omega, e)/dt = K_e(de/dt) + K_\omega(d\omega/dt) \quad (4.5)$$

While relative phase is an inclination-independent measurement, relative eclipse depths depend on e , ω , and i , introducing two constraining equations for three unbound parameters. With high quality photometry, and the addition of concurrent RV measurements, these parameters can be fully constrained by relative eclipse durations. However, in the case of TIC 63459761, the near-resonance of the B period results in interference with one of the two A eclipses, leading to low-confidence depth and width determination over multiple sectors as A_α or A_β ‘eat’ the secondary eclipse. Weighted-average eclipse depths are shown in Table 4.2, though these should be considered as preliminary and tentative.

With TESS data implying, but not strongly binding, variation in e and ω with time, past photometric data were gathered to span a larger temporal baseline. Ground-based survey data, from WASP in 2007, and ASAS-SN from 2015 to today, were reduced and folded to determine relative phase during their time of observation. The phase-folded light curves in Laur, Jaan et al. (2015) and Salas et al. (2014) were also analyzed to give a relative phase for their observation epochs. Comparison of past data confirms the relative consistency of the overall system period, but also reveal rapid evolution in relative eclipse timings, shown in Figure 4.7.

Across this extended observing period, a massive and consistent shift in relative phase is observed, corresponding to an evolution of $f(\omega, e)$ from ~ 0.55 to ~ 0.7 . Traditionally, some

amount of phase shift is attributed to precession of the line of apsides, as ω is correlated with phase. However, as ω also informs relative eclipse depth, the evolution of ω from the 2014 model (phase ~ 0.62) to the current ~ 0.7 would also result in α eclipse depth overtaking β eclipse depth, which is not observed. As such, some amount of eccentric evolution, nonzero (de/dt), must contribute.

The low confidence on the WASP-determined phase is informed by the low SNR of the data, as well as uncertain eclipse attribution. Determining exact eclipse positions is completed by fitting generalized Gaussians, as described in Kostov et al. (2022), to the phase-folded light curve. Figure 4.8 displays the phase-fold of WASP photometry, showing the strongly-expressed β eclipse at a phase of ~ 0.8 . Imposing a second Gaussian fit, with the same width as observed α eclipses in later data, finds a low confidence fit to a phase of ~ 0.25 , with a depth on order with the noise of the data.

While a low confidence determination, either the low expression of α or complete absence of α point towards an evolution of i , alongside e and ω , over a short timescale.

With this host of confounding contributions and rapid evolution, no single effect explains current observations. As such, a combination of variational effects, combined with perturbed dynamical evolution, is likely producing such extreme results. Some possible contributing factors are explored below.

4.2 Variable Contributions

Sections 4.2.1 and 4.2.2 explore a series of possible contributions to the observed out-of-eclipse variations in TIC 63459761, while 4.2.3 summarizes the potential source of eclipse variations. Since the out-of-eclipse variation fails to be explained by a single known effect, it is presumably a combination of multiple periodic contributions, whose magnitude may be enhanced by common resonance.

4.2.1 Ellipsoidal Variations

In close binary systems, individual stars no longer act as idealized oblate spheroids. Rather, they are stretched towards their shared barycenter, resulting in periodic variations as the visible surface area from a given line of sight from each star changes throughout the orbit. In an unperturbed orbit, these variations are consistent between periods, with one lightcurve segment corresponding to the $\alpha \rightarrow \beta$ phase (after α eclipse and before β eclipse) and another the $\beta \rightarrow \alpha$ phase (Morris & Naftilan, 1993). This simple periodicity is not witnessed in the target, but within A, the small separation, high masses, and large relative radii should produce periodic ellipsoidal variations.

The 3rd-harmonic spikes, observable between the third and fourth eclipses in Figure 4.5, are in-line with the heartbeat subcategory of ellipsoidal variations. In so-called heartbeat stars, eccentric orbits result in varying extensions of the ellipsoidal-variation-producing Roche lobes at different phases of the orbit, resulting in an observable spike in magnitude immediately after periapsis (Wrona et al., 2022). Low eccentricity heartbeat stars also produce the visible sawtooth-sinusoid effect seen during the quiescent phase in Figure 4.5. However, for the eccentricities of interest of $e \approx 0.3-0.4$, the amplitude of these effects should be of low order compared to the heartbeat amplitude, which is not observed in the data. The resonance of ellipsoidal effects with close periodicities present within a dynamically interacting system, however, is highlighted in Ou et al. (2023), and presents a potential explanatory path for observed characteristics.

4.2.2 Individual Stellar Variability

Constituent stars themselves are not necessarily constant in time, and internal resonance modes — gravitational [g-] and Rossby-wave [r-] — may also be contributing to observed oscillations. Such g-mode oscillations have been studied within OB-class stars, and do present both the peak-to-peak variational timescale and the longer-term periodic amplitude modulation that would match observation (BursSENS, S. et al., 2020), Figure 5. g-mode driven oscillations dominate in Slowly Pulsating B [SPB] stars, though the current sample of designated SPBs consists of slightly later stars than the constituents of the primary, starting at B2-3V. However, their variational amplitude, and day-order timescale of variation, are in-line with TIC 63459761 Fedurco, M. et al. (2020).

The r-mode oscillations, corresponding to conservation of internal vorticity, have been observed to resonate with g-modes in some tidally-interacting systems, producing quasiperiodic variations that line up with multiples of overall system periodicity, even if not single orbital periods (Witte & Savonije, 1998). Coupled g-r-modes can boost their respective amplitudes, as well, allowing their otherwise minor contribution to be multiplied to observable levels (Degroote, P. et al., 2009). While r-mode and g-mode interactions have been most analyzed in the case of neutron stars, they can be considered outside them as well (Saio et al., 2018).

The combination of various similar-timescale oscillatory effects can produce modulating oscillations with their own unique timescale, which are subject to internal variability through their period. With most effects perturbed or potentially-perturbed on the order of tidal variations, driven by the binary orbit, they may constructively or destructively interfere on a periodic basis longer than their internal variability but consistent with an integer multiple of the perturbing effect (Guo, 2021). Further continuous photometric observations of the target, on timescales greater than 1 month, should be conducted to help bound and isolate this overall periodicity.

4.2.3 Dynamical Evolution

While short-order variations explain baseline modulation, and can induce changes to orbital parameters e and ω , the timescales of these effects are multiple orders of magnitude larger than the timescale of variation observed. However, semistable periodic eccentricity and inclination modulation, on timescales in the 10s of years with the large amplitudes observed, have been theorized as the result of eccentric tertiary perturbers. A case study with abnormal eccentric eclipsing binary DI Herculis by Anderson & Winn (2022) identifies the wide parameter space of i and e variations that pertain to stable orbital solutions for the central binary. These effects are informed by the relative rotational velocities and spin axes of the constituents α and β , and with those undetermined in past Cygnus OB2 rotation surveys, valid tertiary parameter space remains unresolved (Roquette, J. et al., 2017).

It should be noted that the secondary subsystem of TIC 63459761, B_α and B_β , does not exhibit strong ETVs or relative phase variation. Its status as the tertiary perturber is thus questionable; contributions from the individual third star proposed in Kiminki et al. (2007) may be a more likely explanation. In that case, if the two EBs are gravitationally bound and form a QEB, the overall system architecture would be $(2+1)+2$.

4.3 Planned Observations

Previous attempts at characterization of TIC 63459761 used spectral and photometric data gathered from multiple epochs, which produce inconsistencies when combined thanks to the rapid system evolution. Therefore, any observational program of this system must be carefully

planned and coordinated with knowledge of the ephemerides of the full system. It is hoped that a suite of continuous photometric observations over the coming months will coincide with a proposed series of high-resolution spectra (± 100 m/s) via the APO 3.5m spectrograph.

High-resolution spectra over the course of multiple orbits should help separate contributing spectra from major sources, such as the suspected tertiary, from the high-amplitude ($K_\alpha \sim 170$ km/s, $K_\beta \sim 210$ km/s), shifted contributions from the components of system A. From this, rotational velocities and current orientation, and thus current eccentricity, can be constrained, allowing for a complete system characterization.

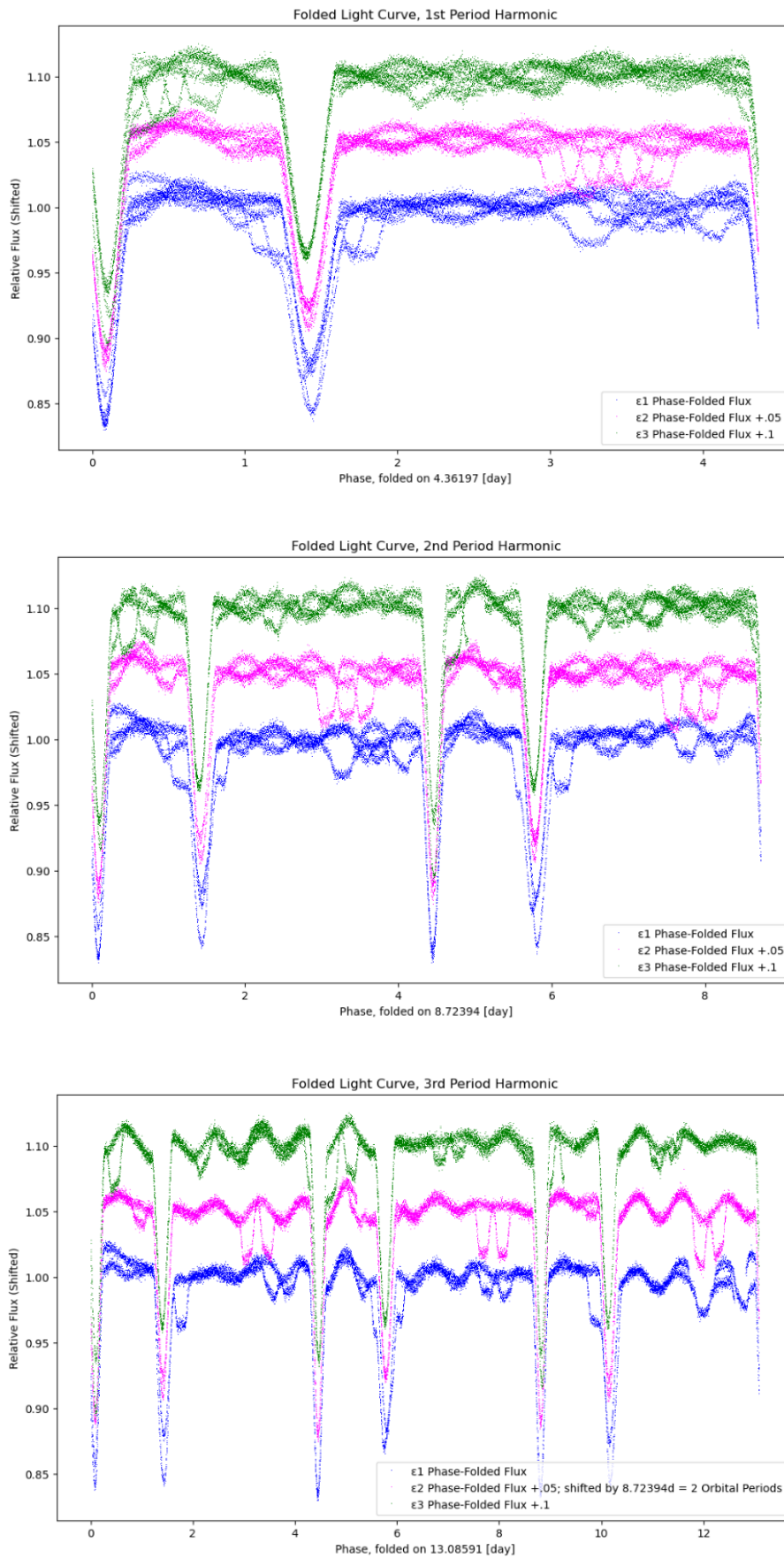


Figure 4.5: TESS phase folded light curves across three epochs, [2021, 2022, 2024]. The 2019 data are excluded due to limited observation length, which prevents phase-folds for longer periods. Pairs of minor dips correspond to eclipses from the B subsystem. Note that while baseline modulations destructively interfere and disagree on primary and secondary harmonic phase folds, they well-align on the third harmonic phase fold, and roughly agree between epochs when an integer period shift is introduced to the second epoch of data.

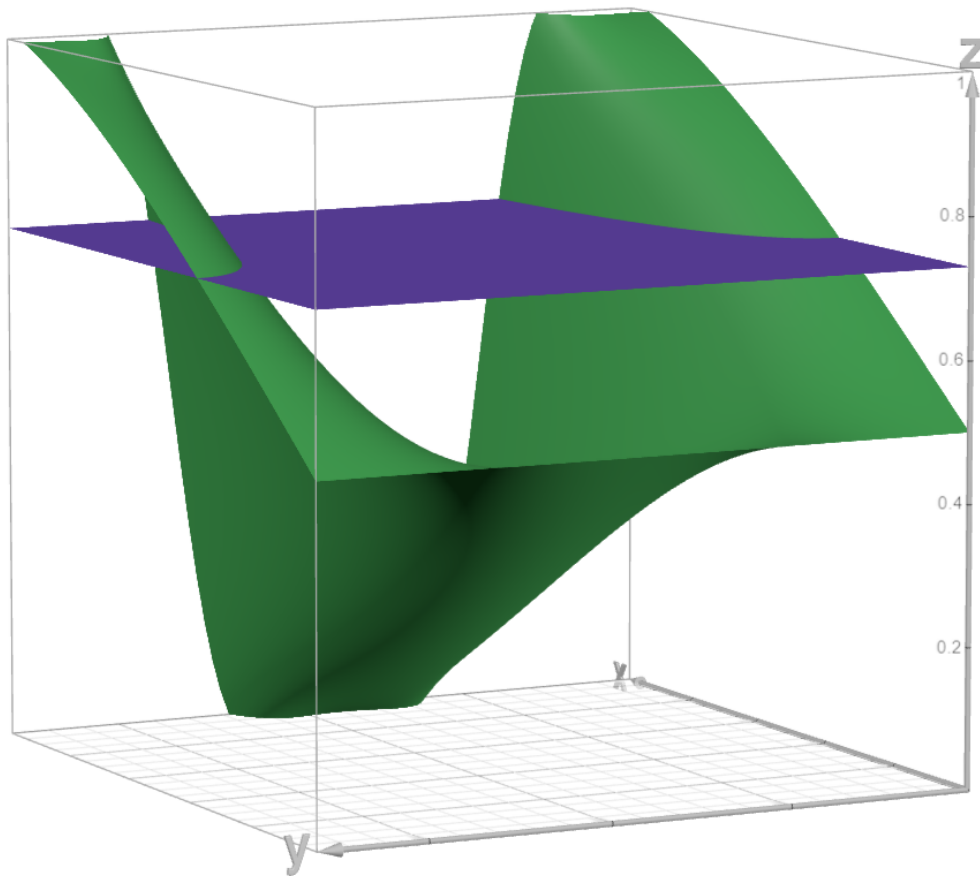


Figure 4.6: Fifth-order expansion of $f(\omega, e)$, with e on the x -axis, over $[0, 1]$, ω on the y -axis, over $[0, 360]$, and f on the z -axis, over $[0, 1]$. The violet plane corresponds to a given observable eclipse phase, and its intersections with the green surface correspond to valid combinations of $\omega; e$. Image generated via Desmos 3D Graphing Calculator, accessible at (<https://www.desmos.com/3d>).

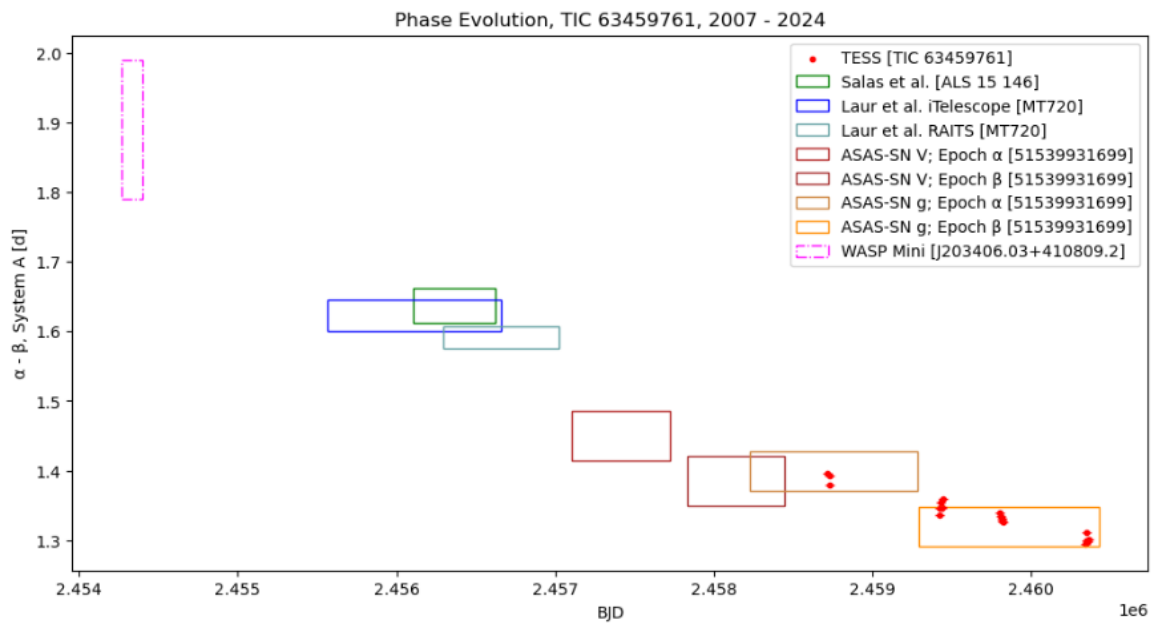


Figure 4.7: Difference, in d , between A_α and A_β across a 17-year time span. The width of the plotted boxes corresponds to the period of the observation, while the height of the boxes corresponds to the uncertainty in eclipse separation. For the long period of ASAS-SN observations, each filter was split into two to reflect more accurately the evolution on that timescale. The dash-dot box representing WASP data is uniquely marked due to its uncertainty. Note directional consistency in subsections of TESS data, either trending up or down within a given sector, suggesting a potential short-term periodic variation alongside the large-scale evolution.

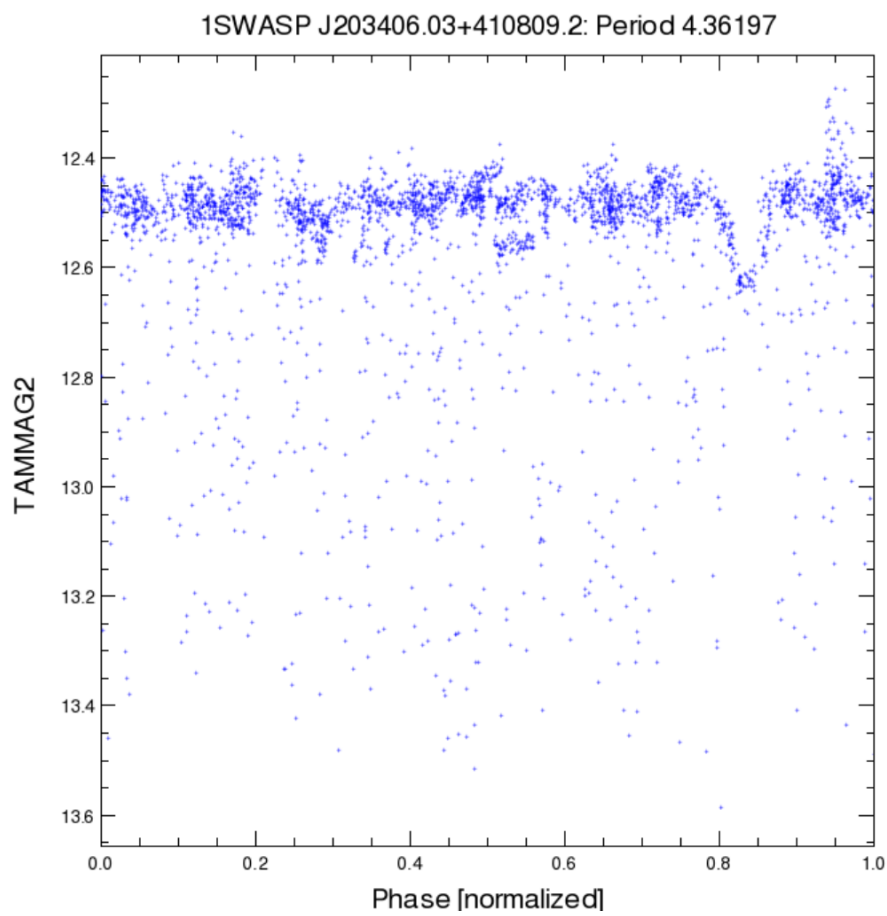


Figure 4.8: WASP phase-folded light curve from 2007 data, via NASA Exoplanet Archive. Note strong expression of β around ~ 0.8 , and potential, but incredibly minor, expression of α around ~ 0.25 .

Section 5

Conclusion

Quadruple Eclipsing Binaries (QEBs) form a small subset of a small subset of a large subset of stellar systems, but are exceptionally revealing specimens to explore dynamical interactions between binary systems. However, they exhibit an expanded degeneracy in confounding variables, while their dynamical interactions can complicate the ephemerides and the predictability of future eclipse timings. As such, they demand special attention through a variety of observational means over long temporal baselines but with short cadences to account for the various variational effects they exhibit. Resonant interactions between these effects can further convolute their characterization.

The following are the key takeaways from this work, by section:

1. Basic QEB Data and Background:

- (a) Ground-based photometry is necessary to identify and correct for potential errors in survey data derived from low angular resolution surveys like *Kepler* and TESS, filling in observation downtime between satellite campaigns.
- (b) The extended, continuous light curves from TESS are necessary to identify out-of-eclipse variations and to produce an initial QEB candidate sample. A synthesis of survey and single-target targeted photometry is thus central to accurate QEB identification, validation, and characterization.
- (c) Diffraction-limited speckle observations can help to partly resolve QEB systems and measure the angular separation between constituent binaries, which, when combined with distance estimates, determine either the projected linear separation of the QEB subsystems or, for QEBs that are not resolved, the maximum projected linear size of the overall system, thereby introducing new constraints on overall architecture.
- (d) Extensive photometry can produce a measure of Eclipse Timing Variations (ETVs) in the form of an (O-C) curve, which can be used to characterize QEB interbinary orbital parameters. These effects should be especially pronounced for compact, speckle-imaging-unresolved systems, which constitute a potentially interesting class for future observation.

2. *Gaia* Distance Discrepancy for QEBs:

- (a) Biases in *Gaia* astrometric solutions for QEB systems resolved with speckle imaging and having an angular separation near *Gaia*'s effective diffraction limit hamper the applicability of parallax-derived distances for such targets. An expanded exploration of *Gaia* systematic errors for samples of known compact binaries may reveal over what range of separations the systematic errors are correlated with separation, and to what degree and how.

3. The Special Case of the QEB TIC 63459761:

- (a) TIC 63459761 constitutes a well-observed, but incompletely-characterized QEB with an eccentric and dynamically-evolving A subsystem. Inconsistencies of past modeling efforts and their failure to completely reproduce observed system parameters suggest the presence of multiple, potentially interacting, perturbative effects within the binary.
- (b) The system's partial, but incomplete, agreement with both binary-induced variations and constituent stellar variability suggest one or more contributing effects, which may be magnified by tidally induced resonances. Variations in eclipse times and depths over a 17-year period suggest significant orbital evolution as well, pointing towards the presence of a tertiary perturbing body aside from the B subsystem.

In coming months, continued photometric observations will be combined with RV measurements of the identified QEB subsample in Section 2, with special attention given to TIC 63459761, to fill out their (O-C) curves and derive overall QEB system parameters. Further speckle observations, including hopefully higher resolution on 8-m class telescopes, alongside with the photometric and spectroscopic data will further explore the *Gaia* biases demonstrated in Section 3.

Section 6

Acknowledgements

This paper makes use of first public release of the WASP data (Butters, O. W. et al., 2010) as provided by the WASP consortium and services at the NASA Exoplanet Archive, which is operated by the California Institute of Technology, under contract with the National Aeronautics and Space Administration under the Exoplanet Exploration Program.

The author would like to thank the consistent assistance of advisor Steven R. Majewski, and collaborators including, but not limited to, James "Jimmy" Davidson and Robert Wilson. Special thanks are extended to Vesselin Kostov, who met to review TIC 63459761 when its abnormalities were identified. Additional thanks for observational help are extended to the staff of Apache Point Observatory, as well as the collaborative review of the UVA Astronomy Department, in specific the graduate student cohort of 2024. This project would not have been possible without their contributions.

Some of our photometry is based on observations obtained with Apache Point Observatory's 0.5-m Astrophysical Research Consortium Small Aperture Telescope.

Some of our photometry is sourced from observations taken through the SKYNET Robotic Telescope Network, developed by Daniel E. Reichart, Joshua B. Haislip, Vladimir V. Kouprianov, Kevin M. Ivarsen, J. Adam Crain, and Andrew C. Foster, using the RRRT, developed by James Davidson, Edward Murphy, and Carlos Salgado.

Bibliography

- Anderson K. R., Winn J. N., 2022, *Were the Obliquities in δ Herculis Excited by an Unseen Tertiary Companion?*, [The Astrophysical Journal](#), 928, 96
- Borucki W. J., et al., 2010, *Kepler Planet-Detection Mission: Introduction and First Results*, [Science](#), 327, 977
- BursSENS, S. et al., 2020, *Variability of OB stars from TESS southern Sectors 1–13 and high-resolution IACOB and OWN spectroscopy*, [Astronomy & Astrophysics](#), 639, A81
- Butters, O. W. et al., 2010, *The first WASP public data release*, [Astronomy & Astrophysics](#), 520, L10
- Collins K. A., Kielkopf J. F., Stassun K. G., Hessman F. V., 2017, *AstroImageJ: Image Processing and Photometric Extraction for Ultra-Precise Astronomical Light Curves*, [The Astronomical Journal](#), 153, 77
- Dainty J., 1981, *Speckle interferometry in astronomy*, *Recent Advances in Observational Astronomy*, pp 95–109
- Degroote, P. et al., 2009, *Evidence for nonlinear resonant mode coupling in the β Cephei star HD180642 (V1449 Aquilae) from CoRoT photometry*, [Astronomy & Astrophysics](#), 506, 111
- Eggleton P. P., Tokovinin A. A., 2008, *A catalogue of multiplicity among bright stellar systems*, [Monthly Notices of the Royal Astronomical Society](#), 389, 869
- Fabrizius, C. et al., 2021, *Gaia Early Data Release 3 - Catalogue validation*, [Astronomy & Astrophysics](#), 649, A5
- Fang X., Thompson T. A., Hirata C. M., 2018, *Dynamics of quadruple systems composed of two binaries: stars, white dwarfs, and implications for Ia supernovae*, [Monthly Notices of the Royal Astronomical Society](#), 476, 4234
- Fedurco, M. Paunzen, E. Hümmerich, S. Bernhard, K. Parimucha, Š. 2020, *Pulsational properties of ten new slowly pulsating B stars*, [Astronomy & Astrophysics](#), 633, A122
- Gaia Collaboration et al., 2018, *Gaia Data Release 2 - Summary of the contents and survey properties*, [Astronomy & Astrophysics](#), 616, A1
- Gaia Collaboration et al., 2023, *Gaia Data Release 3 - Summary of the content and survey properties*, [Astronomy & Astrophysics](#), 674
- Greenaway A., 1981, *Isoplanatism in Speckle Interferometry and Adaptive Optics*, *Solar instrumentation: What's next?*, pp 403–420
- Guo Z., 2021, *Asteroseismology of Close Binary Stars: Tides and Mass Transfer*, [Frontiers in Astronomy and Space Sciences](#), 8, 67

- Hedges C., 2021, *Vetting: A Stand-alone Tool for Finding Centroid Offsets in NASA Kepler, K2, and TESS, Alerting the Presence of Exoplanet False Positives*, [Research Notes of the AAS](#), 5, 262
- Høg E., et al., 2000, *The Tycho-2 catalogue of the 2.5 million brightest stars*, [Astronomy & Astrophysics](#), 355, L27
- Horch E., Veillette D., Baena Gallé R., Shah S., O’Rielly G., Altena a., 2009, *Observations of Binary Stars with the Differential Speckle Survey Instrument. I. Instrument Description and First Results*, [The Astronomical Journal](#), 137, 5057
- Kiminki D. C., et al., 2007, *A Radial Velocity Survey of the Cyg OB2 Association*, [The Astrophysical Journal](#), 664, 1102–1120
- Kiminki D. C., McSwain M. V., Kobulnicky H. A., 2008, *New Massive Binaries in the Cygnus OB2 Association*, [The Astrophysical Journal](#), 679, 1478
- Kiminki D. C., et al., 2012, *Additional Massive Binaries in the Cygnus OB2 Association*, [The Astrophysical Journal](#), 747, 41
- Kobulnicky H. A., et al., 2014, *Toward Complete Statistics of Massive Binary Stars: Penultimate Results from the Cygnus OB2 Radial Velocity Survey*, [The Astrophysical Journal](#), 213, 34
- Kochanek C. S., et al., 2017, *The All-Sky Automated Survey for Supernovae (ASAS-SN) Light Curve Server v1.0*, [Publications of the Astronomical Society of the Pacific](#), 129, 104502
- Kostov V. B., et al., 2021a, *TIC 454140642: A Compact, Coplanar, Quadruple-lined Quadruple Star System Consisting of Two Eclipsing Binaries*, [The Astrophysical Journal](#), 917, 93
- Kostov V. B., et al., 2021b, *TIC 454140642: A Compact, Coplanar, Quadruple-lined Quadruple Star System Consisting of Two Eclipsing Binaries*, [The Astrophysical Journal](#), 917, 93
- Kostov V. B., et al., 2022, *Ninety-seven Eclipsing Quadruple Star Candidates Discovered in TESS Full-frame Images*, [The Astrophysical Journal Supplement Series](#), 259, 66
- Kostov V. B., et al., 2023, *101 eclipsing quadruple star candidates discovered in TESS full frame images*, [Monthly Notices of the Royal Astronomical Society](#), 527, 3995
- Laur, Jaan Tempel, Elmo Tuvikene, Taavi Eenmäe, Tõnis Kolka, Indrek 2015, *Period change of massive binaries from combined photometric and spectroscopic data in Cygnus OB2*, [Astronomy & Astrophysics](#), 581, A37
- Magliano C., et al., 2023, *The TESS Triple-9 Catalog II: a new set of 999 uniformly vetted exoplanet candidates*, [Monthly Notices of the Royal Astronomical Society](#), 521, 3749–3764
- Mardling R. A., Aarseth S. J., 2001, *Tidal interactions in star cluster simulations*, [Monthly Notices of the Royal Astronomical Society](#), 321, 398
- Massey P., Thompson A. B., 1991, *Massive Stars in CYG OB2*, [The Astrophysical Journal](#), 101, 1408
- Meredith K., Haislip J., Reichart D., 2020, *Afterglow Access – Progress Report on the Development of Accessible Data Analysis Software for Astronomy for BVI (Blind and Visually Impaired) Students and Astronomers*, American Astronomical Society Meeting Abstracts, 235, 136.06

- Morris S. L., Naftilan S. A., 1993, *The Equations of Ellipsoidal Star Variability Applied to HR 8427*, [The Astrophysical Journal](#), 419, 344
- Ou J.-W., Jiang C., Yang M., Yu C., Gao D.-Y., Long G., 2023, *Tidal Resonance: A Factor Worth Considering in the Orbital Evolution of Heartbeat Stars*, [Universe](#), 9, 514
- Prša A., et al., 2011, *Kepler Eclipsing Binary Stars. I. Catalog and Principal Characterization of 1879 Eclipsing Binaries in the First Data Release*, [The Astrophysical Journal](#), 141, 83
- Rate G., Crowther P. A., Parker R. J., 2020, *Unlocking Galactic Wolf–Rayet stars with Gaia DR2 – II. Cluster and association membership*, [Monthly Notices of the Royal Astronomical Society](#), 495, 1209–1226
- Ricker G. R., et al., 2015, *Transiting Exoplanet Survey Satellite (TESS)*, [Journal of Astronomical Telescopes, Instruments, and Systems](#), 1, 014003
- Roquette, J. Bouvier, J. Alencar, S. H. P. Vaz, L. P. R. Guarcello, M. G. 2017, *Near-infrared time-series photometry in the field of Cygnus OB2 association - I. Rotational scenario for candidate members*, [Astronomy & Astrophysics](#), 603, A106
- Saio H., Kurtz D. W., Murphy S. J., Antoci V. L., Lee U., 2018, *Theory and evidence of global Rossby waves in upper main-sequence stars: r-mode oscillations in many Kepler stars*, [Monthly Notices of the Royal Astronomical Society](#), 474, 2774
- Salas J., Apellániz J. M., Barbá R. H., 2014, *A photometric variability study of massive stars in Cygnus OB2*, [Highlights of Spanish Astrophysics VIII](#)
- Salgado C., McDavid D., 2008, *The Rapid Response Robotic Telescope (RRRT) at Fan Mountain Observatory, Virginia*, American Astronomical Society Meeting Abstracts, 212, 24.02
- Sana H., et al., 2012, *Binary Interaction Dominates the Evolution of Massive Stars*, [Science](#), 337, 444
- Sterne T. E., 1939, *Apsidal Motion in Binary Stars (II) Distributions of Density*, [Monthly Notices of the Royal Astronomical Society](#), 99, 662
- Tokovinin A., 2014, *From binaries to multiples II: hierarchical multiplicity of F and G dwarfs*, [The Astronomical Journal](#), 147, 87
- Tokovinin A., 2021, *Architecture of Hierarchical Stellar Systems and Their Formation*, [Universe](#), 7
- Tokovinin A., Horch E. P., 2016, *Speckle interferometry of secondary components in nearby visual binaries*, [The Astronomical Journal](#), 152, 116
- Torres G., Andersen J., Giménez A., 2009, *Accurate masses and radii of normal stars: modern results and applications*, [The Astronomy and Astrophysics Review](#), 18, 67–126
- Witte M., Savonije G., 1998, *The dynamical tide in a rotating 10 Ms main sequence star. A study of g- and r-mode resonances*, [Astronomy & Astrophysics](#), 341, 842
- Wrona M., et al., 2022, *The OGLE Collection of Variable Stars: One Thousand Heartbeat Stars in the Galactic Bulge and Magellanic Clouds*, [The Astrophysical Journal Supplement Series](#), 259, 16

-
- Zasche, P. Wolf, M. Vraštil, J. Pilarčík, L. Juryšek, J. 2016, *The first study of the light-travel time effect in massive LMC eclipsing binaries*, [Astronomy & Astrophysics](#), 590, A85
- Zasche, P. et al., 2019, *Doubly eclipsing systems*, [Astronomy & Astrophysics](#), 630, A128